

Incorporating Nanoscale Effects into a Continuum-Scale Reactive Transport Model for CO₂-Deteriorated Cement

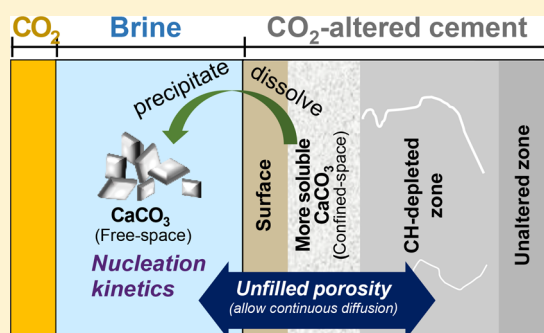
Qingyun Li,[†] Carl I. Steefel,[‡] and Young-Shin Jun^{*,†}

[†]Department of Energy, Environmental and Chemical Engineering, Washington University, Saint Louis, Missouri 63130, United States

[‡]Energy Geosciences Division, Lawrence Berkeley National Laboratory, Berkeley, California 94720, United States

S Supporting Information

ABSTRACT: Wellbore cement deterioration is critical for wellbore integrity and the safety of CO₂ storage in geologic formations. Our previous experimental work highlighted the importance of the portlandite (CH)-depleted zone and the surface dissolution zone in the CO₂-attacked cement. In this study, we simulated numerically the evolution of the CH-depleted zone and the dissolution of the cement surfaces utilizing a reduced-dimension (1D) reactive transport model. The approach shows that three nanoscale effects are important and had to be incorporated in a continuum-scale model to capture experimental observations: First, it was necessary to account for the fact that secondary CaCO₃ precipitation does not fill the pore space completely, with the result that acidic brine continues to diffuse through the carbonated zone to form a CH-depleted zone. Second, secondary precipitation in brine begins via nucleation kinetics, and this could not be described with previous models using growth kinetics alone. Third, our results suggest that the CaCO₃ precipitates in the confined pore space are more soluble than those formed in brine. This study provides a new platform for a reduced dimension model for CO₂ attack on cement that captures the important nanoscale mechanisms influencing macroscale phenomena in subsurface environments.



INTRODUCTION

The integrity of wellbore cement is crucial to ensure the safety and efficiency of geologic CO₂ sequestration (GCS) because the chemical reactions of cement with injected CO₂ can lead to the opening of high-porosity zones and fractures, potentially forming CO₂ leakage pathways.^{1,2} Therefore, deterioration of wellbore cement under GCS conditions has been investigated intensively in the past decade.^{3–13} These previous studies include both experimental and modeling approaches and have been conducted on both chemical and mechanical alteration of cement. By adding the new scenario of GCS, the findings of these studies extend our understanding of the century-old topic of cement deterioration. The GCS environments are commonly characterized by a greater amount of CO₂, higher temperature, higher pressure, and higher salt concentration than in the common cement operating environments.³ Chemical reactions occurring in cement under GCS conditions produce several zones in cement matrices. Upon exposure to CO₂-saturated acidic brine, Ca²⁺ ions are released from dissolution of portlandite (Ca(OH)₂, or CH for short) in the cement matrices.³ The dissolution of CH results in a CH-depleted zone with enhanced porosity. As the Ca²⁺ ions diffuse out and encounter carbonate ions from CO₂-saturated brine, a carbonated layer is formed. To some extent, the carbonated layer can protect the cement by hindering CO₂ diffusion into the inner cement part. On the outer front of this carbonated

layer, the acidic brine continues to dissolve CaCO₃, leading to a surface dissolution layer with enhanced porosity.^{3,9}

In addition to characterizing chemical reactions that take place during GCS, several studies have focused on the (hydro)mechanical property changes of cement after CO₂ exposure.^{5,6,10,11,13–26} In our recent study,¹¹ we found that two important zones in CO₂-attacked cement are related to the decrease of cement strength and, thus, deserve more attention. One is the wide and weak CH-depleted zone, characterized by increased porosity due to dissolution of CH. The CH-depleted zone has also been observed in previous studies and, in some cases, was noticeably wide.^{4,11,22,24–27} However, the factors that control the widening of this zone during the reaction are not clear, and thus, it is uncertain how the width of this zone can be limited for designing a better wellbore cement material.

The other reaction zone is the surface layer due to dissolution of the outer part of the carbonated layer. Intense dissolution of the outer front of the carbonated layer makes it thinner and reduces its effectiveness in blocking CO₂ from diffusing into the cement. If the cement deteriorates in a flow-through system,^{13,16–19,22,24,28–32} with fresh solutions under-

Received: February 2, 2017

Revised: July 30, 2017

Accepted: August 7, 2017

Published: August 7, 2017

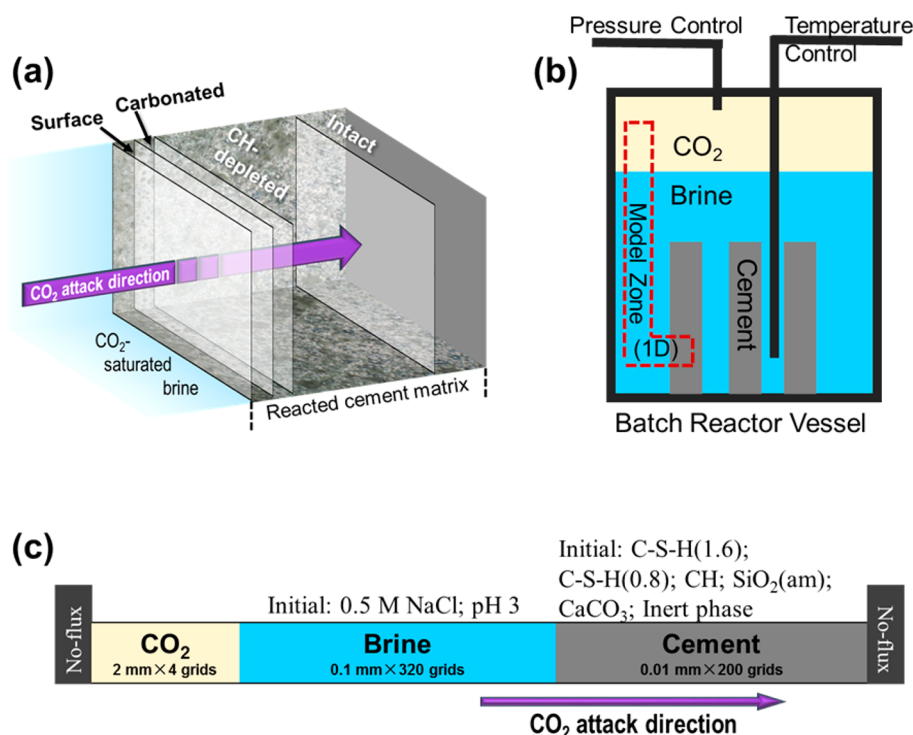


Figure 1. Illustration of experimental observations and our modeling setup. (a) Illustration of direction of CO₂ attack into the cement matrix based on the 10 day reaction system. A total alteration thickness of $1220 \pm 90 \mu\text{m}$ was observed, including a $960 \mu\text{m}$ CH-depleted zone, a $100 \mu\text{m}$ carbonated layer, and a $170 \mu\text{m}$ surface region. Interfaces between zones are drawn to scale. In both this and our previous study,¹¹ we observed that the CO₂ attack and associated reaction fronts were along one direction and, thus, effectively one-dimensional. (b) Diagram of the experimental reactor. A total of eight pieces of cement were reacted in one reactor, but only three are drawn for illustration. The dotted line encloses the region where the domains and their relative volume ratios are captured in the 1D model shown in panel c. (c) Discretization of the reactive transport model in 1D. The arrow shows the CO₂ attack direction corresponding to the illustration in panel a.

saturated with CaCO₃ continuously injected, it is intuitive that the surface of the cement samples can dissolve. However, in a closed system,^{9–12,14,15,23,25,26,33–36} the solution can quickly become saturated with CaCO₃ due to CH dissolution. One would expect that the outer front of the carbonated layer would not dissolve once its saturation is reached, but our experimental observations show that it continues to dissolve. If protective strategies of wellbore cement are to reduce the dissolution of the carbonated layer, it is necessary to elucidate the mechanisms that cause the dissolution.

To analyze the effects of various conditions (such as temperature, pressure, chemistry, and flow rates) on cement deterioration within reasonable time and resources, reactive transport modeling has been employed at both the continuum^{4,5,7,8,37–41} and the pore scales.⁴² However, previous focus has been on the overall depth of attack or the carbonated layer's inner front,^{4,5,7,8} while the CH-depleted zone and the surface layer have not been sufficiently considered. A few modeling studies were able to predict the CH-depleted zone and a surface dissolution layer but only with open boundaries in which the reactive solution in contact with the cement is replenished, and the chemical composition remains constant or nearly so.^{4,5,8,27,39,40,42} In the natural subsurface environment, however, the aqueous concentrations are allowed to evolve when the fluid is confined in a relatively stagnant system without flow,⁴³ such as in abandoned wells or in cement microcracks in operating wells.

In contrast to the previous reactive transport models mentioned above, the focus of this study is to develop a continuum-scale reactive transport model with more-realistic

boundary conditions with respect to the experimental study. This modeling study focuses on the evolution of the CH-depleted zone and the surface dissolution zone. The reactive transport modeling software CrunchTope (a new version of CrunchFlow)⁴⁴ was employed for this work. In addition, careful consideration of nanoscale mechanisms (such as nucleation and precipitation in a confined pore space) was included in this study. Whether these effects need to be included in models was not clear in the past because they mostly have not been considered in previous models. However, these mechanisms appear to play a more general role in many reactive transport processes. For example, nucleation of a new mineral phase provides new reactive surface area, and precipitation in confined pores can determine the permeability and diffusivity of a geomedium. Based on experimental observations, these mechanisms are important in our system, and therefore, we have explored their importance by incorporating them into the numerical model. The three major nanoscale mechanisms we considered are the ineffectiveness of secondary precipitation in completely filling pore space, the nucleation of minerals to initiate secondary precipitation, and a more-soluble carbonate formation in pore confinement.

■ APPROACHES

Experimental Approach. This modeling work is based on an experimental study published by Li et al. (2015)¹¹ with additional tests for time-resolved observations. The experiments were carried out using laboratory-made Ordinary Portland Cement (OPC, the basis for all other types of Portland cement).⁴⁵ The cement samples were reacted in a

Table 1. Reactions and Parameters for Reactive Transport Modeling of Cement Deterioration at 95 °C and Initial Conditions for Cement and Brine Domains in the Model^a

speciation reactions (instantaneous)		precipitation/dissolution reactions				
reaction	$\log_{10} K_{eq}$	mineral	reaction	$A_{ss} \times k a_{H^+}^n$	$\log_{10} K$	
$H_2O \leftrightarrow H^+ + OH^-$	-12.33	CaCO ₃ _in_cement CaCO ₃ _in_brine	$CaCO_3 + H^+ \leftrightarrow Ca^{2+} + HCO_3^-$	$10^{-3.0} a_{H^+}^{0.7}$	1.0527	
$CO_2(aq) + H_2O \leftrightarrow H^+ + HCO_3^-$	-6.358				0.8527	
$HCO_3^- \leftrightarrow H^+ + CO_3^{2-}$	-10.08	CH	$Ca(OH)_2 \leftrightarrow Ca^{2+} + 2OH^-$	$10^{-5.0}$	18.51	
$CaCl_2(aq) \leftrightarrow Ca^{2+} + 2Cl^-$	0.4445	C-S-H(1.6)	$C-S-H(1.6) + 3.2H^+ \leftrightarrow 1.6Ca^{2+} + SiO_2(aq) + 4.18H_2O$	$10^{-7.8}$	23.70	
$CaCl^+ \leftrightarrow Ca^{2+} + Cl^-$	-0.1696	C-S-H(0.8)	$C-S-H(0.8) + 1.6H^+ \leftrightarrow 0.8Ca^{2+} + SiO_2(aq) + 2.3H_2O$		9.538	
$CaCO_3(aq) + H^+ \leftrightarrow Ca^{2+} + HCO_3^-$	6.165	SiO ₂ (am)	$SiO_2(am) \leftrightarrow SiO_2(aq)$	$10^{-6.5}$	-2.191	
$CaHCO_3^+ \leftrightarrow Ca^{2+} + HCO_3^-$	-1.140					
$CaOH^+ + H^+ \leftrightarrow Ca^{2+} + H_2O$	10.24					
$HCl(aq) \leftrightarrow H^+ + Cl^-$	-0.6262					
$HSiO_3^- + H^+ \leftrightarrow H_2O + SiO_2(aq)$	9.134					
$NaCl(aq) \leftrightarrow Na^+ + Cl^-$	0.4979					
$NaHSiO_3 + H^+ \leftrightarrow H_2O + Na^+ + SiO_2(aq)$	7.849					
$NaOH(aq) + H^+ \leftrightarrow Na^+ + H_2O$	12.99					
$NaCO_3^- + H^+ \leftrightarrow HCO_3^- + Na^+$	10.55					
$NaHCO_3(aq) \leftrightarrow HCO_3^- + Na^+$	0.3712					
initial condition for cement						
composition	C-S-H(1.6)	C-S-H(0.8)	CH	SiO(am)	CaCO ₃ _in_cement	inert
volume fraction	0.31	0.05	0.16	0.01	0.00001	0.27
initial condition for brine						
composition	NaCl(M)	pH	inert teflon (volume fraction)		CaCO ₃ _in_brine (volume fraction)	
value	0.5	3.0	0.01 for selective grid cells		none	

^aThermodynamic parameters are from the EQ3/6 database⁴⁸ and the Thermoddem database.⁴⁹ Kinetic parameters are calibrated with our experimental observations within ranges reported in the literature.^{4,5,7,40,41,73–75}

CO₂-saturated brine (0.5 M NaCl) with a solid-to-liquid volume ratio of 1:16. The solution was equilibrated at 95 °C under 100 ± 5 bar of CO₂ in the headspace of the stagnant batch reactor. In our previous experimental study, the reaction extended over 10 days, and a total alteration thickness of 1220 ± 90 μm was observed, including a 960 μm CH-depleted zone, a 100 μm carbonated layer, and a 170 μm surface region. To obtain the evolution of each zone along the reaction time, additional batch experiments were conducted for 1, 3, and 6 days in this study. After the reaction, polished cross-sections of the reacted samples were observed using an optical microscope (Zeiss Imager microscope), and the depths of the individual fronts were recorded. More information on the experimental setup, the characterization of aqueous and solid phases, and discussion of the results can be found in our previous publications.^{11,26,76}

After 6 and 10 days of reaction, secondary CaCO₃ precipitates were detected in the reaction solution. These precipitates were collected and ground to powder samples for characterization using X-ray diffraction (XRD, Bruker D8 Advance). The carbonated layer (formed due to secondary precipitates) in the cement matrix was also ground for XRD characterization. More information and discussion on this secondary phase and on the XRD tests can be found in the Supporting Information.

Reactive Transport Model Setup. In the experiments, we observed that the interfaces among reaction zones in the cement matrix were distinct and parallel to the brine-cement interface (as illustrated in Figure 1a). The optical microscopic images in Figure S2 indicated that the CO₂ attack propagated into the cement matrix primarily along the axis perpendicular to the brine-cement interface. Based on the larger scale geometry of the alteration fronts, it is reasonable to assume a 1D geometry, as shown in Figure 1, although multidimensional effects are possible (and expected) at the pore scale. In addition, the 1D approach is computationally more efficient, an advantage when one wants to consider multiple scenarios to explain the experimental observations. Based on these observations, we set up a 1D continuum model using the CrunchTope software.⁴⁴ Figure 1b,c illustrates the connection between the experimental setup and model domains. The L-shaped area enclosed by dotted lines in Figure 1b shows the phase domains and their qualitative volume ratios and spatial relationship established in our 1D numerical model, as schematized in Figure 1c. Our model has no-flux (closed) boundaries that allow evolution of aqueous concentrations within the reactive brine and cement and accurately reflects the solid-to-liquid ratio and initial and boundary conditions used in the experiment.

Discretization. The 1D model has three domains, including the headspace of supercritical CO₂ on the left (2 mm × 4

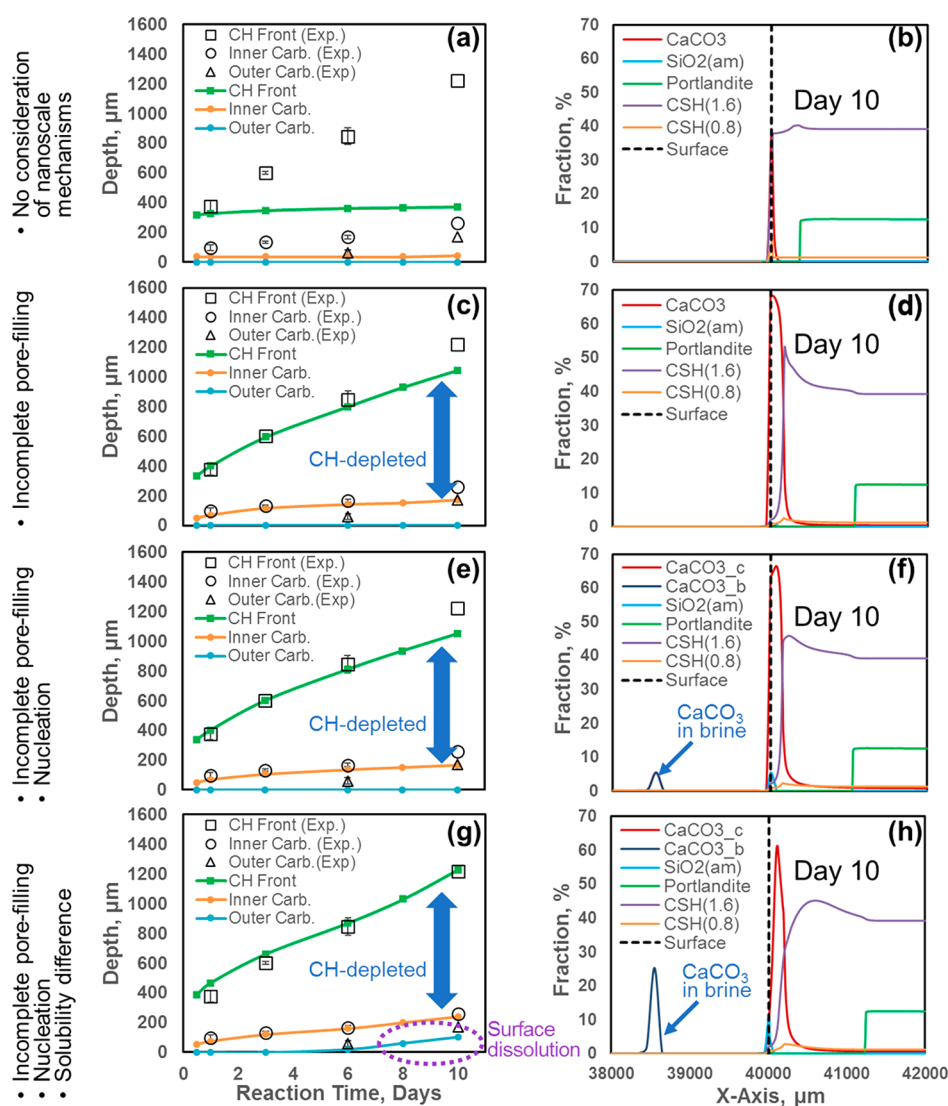


Figure 2. Modeling results without and with sufficient consideration of nanoscale mechanisms in comparison with experimental data. The left column of figures shows the time-resolved modeling results and their consistency with experimental observations. The right column of figures shows the mineral fraction profiles at day 10 as an example time point, in correspondence with the time-resolved results on the left. (a,b) Results with no consideration of nanoscale mechanisms. (c,d) Results with consideration of incomplete filling of pore space at nanoscale. The CH-depleted zone is reproduced with this consideration. (e,f) Results with additional consideration of nucleation kinetics. Secondary precipitates are predicted in brine. (g,h) Results with additional consideration of enhanced solubility in confined-pores. More secondary precipitation in brine is predicted, and the surface dissolution zone is reproduced. These results match well with experimental observations.

grids), the CO_2 -saturated brine ($100 \mu\text{m} \times 320$ grids) in the middle, and the cement paste ($10 \mu\text{m} \times 200$ grids) on the right. Initial pressure in all domains was 100 bar, and the volume ratio of cement to brine was 1:16, reflecting that used in the experiment. To facilitate CO_2 dissolution into brine, the CO_2 domain also includes 1 vol % of brine. As calculated using Duan's equation of state,⁴⁶ the CO_2 fugacity decreased from 85 to 77 bar at the first grid of the brine domain as a result of consumption of CO_2 by chemical reactions throughout the 10 day experiment. The CO_2 fugacity was considered stable because it was similar to the pressure fluctuation in the experiment.

Governing Equation. In CrunchTope, the governing equation that couples the chemical reactions and mass transport is

$$\frac{\partial(\phi C_i)}{\partial t} = \frac{\partial}{\partial x} \left(D_{ie} \frac{\partial C_i}{\partial x} \right) - \frac{\partial}{\partial x} (\phi u C_i) + \sum_{r=1}^N \nu_{ir} R_{ir} \quad (1)$$

In this equation, ϕ is porosity, C_i is the concentration for species i , and t is the time. The change of bulk concentration of species i with time (described by the left side) is expressed by three terms on the right side, including a diffusion term, an advection term, and a reaction term, from left to right, respectively. D_{ie} is the effective diffusivity of species i , x is the dimension axis, u is the average linear velocity of the fluid, ν_{ir} is the stoichiometric coefficient of the reaction that involves species i , and R_{ir} is the reaction rate for species i in the r th reaction. In our stagnant system, the advection term is negligible, and eq 1 is left with the diffusion and reaction terms on the right side.

Transport. The effective diffusion coefficient D_{ie} in eq 1 was calculated from the diffusion coefficient D_i , corrected for tortuosity and porosity according to Archie's law:

$$D_{ie} = \phi^m D_i \quad (2)$$

where ϕ is the porosity and m is the cementation exponent.^{44,47} The coefficient D_i was assumed to be $3 \times 10^{-9} \text{ m}^2/\text{s}$ for all species at 95 °C. This simplification is reasonable because the diffusivities of all relevant ions are in the range of $10^{-9} \text{ m}^2/\text{s}$, and specifying diffusivity for individual ions did not alter the final results significantly (see Figure S3 and Table S2 for more information). The value for m was set as 2 in this study as suggested for systems without further information about m .⁴⁷ Unless the minimum transport porosity was reached (see the following section), the porosity was updated at every time step by subtracting the total mineral fractions from 100%:⁴⁴

$$\phi = 1 - \sum_j \phi_{mj} \quad (3)$$

where ϕ_{mj} is the volume fraction of mineral j .

Chemical Reactions. Chemical reactions include thermodynamic-controlled speciation reactions and kinetic-controlled dissolution/precipitation reactions. Parameters are listed in Table 1. Most of the thermodynamic parameters are from the EQ3/6 database,⁴⁸ with the exception of those for C–S–H phases, which are from the Thermoddem Database.⁴⁹ The kinetic rate equations for dissolution/precipitation, except for nucleation reactions, are based on transition state theory (TST)⁵⁰ and are written as

$$R = A k a_{\text{H}^+}^n \left(1 - \frac{\text{IAP}}{K_{\text{sp}}} \right) \quad (4)$$

In this equation, A is the surface area (calculated as the product of the mineral's mass and its specific surface area A_{ss}), k is the rate constant, a_{H^+} is the activity of H^+ , n is the dependence of the rate on the hydrogen ion activity, IAP is the ion activity product, and K_{sp} is the solubility product of the reacting mineral. The values for A_{ss} and k are available in the literature, each with large ranges; therefore, to be efficient, the product of $A_{\text{ss}} \cdot k$ is treated as one parameter. The values used in this study are calibrated within literature-reported ranges to best match our experimental results.⁵¹

Initial Conditions. To simulate CO_2 attack on Portland cement, the hydrated cement composition can be simplified to include only CH and C–S–H, and small amounts of amorphous SiO_2 and CaCO_3 .^{37,52} This simplification is valid because other components, such as Fe- and Al-containing hydrated phases, are much less abundant than the CH and C–S–H phases and their reactions with CO_2 do not contribute significantly to cement deterioration.^{9,45,52} In cement, C–S–H exists as a semi-amorphous gel with a spectrum of ratios of calcium to silicon.⁴⁵ We included two of the compositions, denoted as C–S–H(1.6), with a higher Ca-to-Si atom ratio of 1.6, and C–S–H(0.8), with a lower Ca-to-Si atom ratio of 0.8. For the CaCO_3 phase, to avoid unnecessary confusion with CaCO_3 phase transformations, we utilized parameters for calcite ($K_{\text{sp}} = 10^{-9.23}$ at 95 °C), following common procedure in cement modeling,^{4,7,8,33,39} with the exception that an additional “calcite” phase with slightly higher solubility was also included as one of the nanoscale mechanisms discovered in this study.

For the initial condition in the cement domain, we assumed the majority of the cement reactive phases were made up of 36% C–S–H(1.6) and 16% CH, with 5% of C–S–H(0.8) possibly from hydration at low-Ca zones, a 1% SiO_2 component from incomplete reaction with CH to form C–S–H, and <0.1% CaCO_3 from unavoidable exposure to atmospheric CO_2 during cement hardening and hydration. The amounts of C–S–H(1.6) and CH were determined from previously reported X-ray fluorescence (XRF) results on OPC powder before hydration.¹¹ Details can be found in section S2 of the Supporting Information.

The initial condition for the solution domain was set according to that used in the experiments. The solution contained 0.5 M of NaCl. Ion activity coefficients were calculated using the extended Debye–Hückel (i.e., B-dot) equation, with the exception of $\text{CO}_2(\text{aq})$, which the Duan equation of state calculates more accurately than conventional activity coefficient models.⁴⁶ The initial pH of the solution was set as 3.0 to be consistent with our experimentally measured initial pH (3.0 ± 0.1), and Cl^- was used as the charge-balancing species. The initial compositions of the brine and the cement domains in our 1D model are summarized in Table 1.

RESULTS AND DISCUSSION

Experimental Observations. Optical images of cement cross-sections reacted with CO_2 for 1, 3, 6, and 10 days are shown in Figure S2. Consistent with the literature,^{3,9} layered structures formed in the cement matrix, including a CH-depleted zone, a carbonated layer, and a surface layer. The front depths are plotted in Figure 2. The CH front propagates quickly and almost linearly with reaction time, while the inner front of the carbonated layer moves much more slowly into the inner matrix of cement. This suggests that even after the carbonated layer was formed, there was still diffusion of acidic brine through the carbonated layer that continued to dissolve the CH front. Even at the longest reaction time, we observed only a few of the total cement samples with microcracks on the surface, and yet all samples had similar widths of the CH-depleted zones.¹¹ Hence, these microcracks cannot be the major explanation for diffusion through the carbonate layer.

Further, the dissolved surface layer was not observable in day-1 and day-3 samples but was obvious in the day-6 and day-10 samples. Correspondingly, in day-6 and day-10 systems, secondary CaCO_3 precipitates were observed in brine (see section S1 in the Supporting Information for more discussion on the secondary precipitates). This correspondence in time suggests that the dissolution of the cement surface is associated with the secondary precipitation in brine.

In the following, we present the results of reactive transport simulations of CO_2 -deteriorated cement, beginning with the “base case” in which the conventional continuum approaches as described in the Reactive Transport Model Setup section are used, and progressing to incorporation of three nanoscale mechanisms so as to capture the experimental observations in which the base case fails. The modeling results without and with consideration of the nanoscale mechanisms are presented in Figure 2.

Base Case Continuum Model. In the “base case” treatment, the mathematical formulations described in eqs 1–4 are used to simulate the CO_2 deterioration of the cement. The simulations based on a conventional continuum treatment of the reactive cement system predict that complete closing of the pore space by CaCO_3 precipitation will prevent acidic CO_2

from diffusing to the CH front, thus effectively arresting its propagation (Figure 2a,b). In continuum-scale models, the porosity of the medium as it evolves is often calculated using eq 3. If minerals continue to precipitate, the porosity will continue to decrease until it approaches zero ($\phi \approx 10^{-4}$). Because this near-zero-porosity zone limits diffusion of the reactive fluid into the cement according to eq 2, the precipitation will slow down due to lack of reactants (primarily CO_2 in this case) reaching the precipitating zone in cement. Furthermore, the CaCO_3 on the surface of the cement does not dissolve to form a surface dissolution zone because the brine in contact with the cement surface is already oversaturated with CaCO_3 (Figure S4c). These discrepancies from observations could not be resolved by merely altering parameters in the base case model.

Lack of Complete Pore Filling in Carbonated Layer. In both natural and engineered porous media, it has been reported that mineral precipitation does not always completely fill the entire pore distribution.⁵³ The experimental observations of our cement system also suggest that the carbonate layer is a zone that experienced incomplete filling of the pore space, although extensive CaCO_3 precipitation clearly took place and there is no observable pore space in microscopic images (Figure S2). This less-than-complete filling of all of the porosity by the carbonated layer can be attributed to defects in the carbonated layer and/or pore-size-dependent precipitation. As can be observed in the optical images in Figure S2, the carbonated layer has ragged fronts. If the carbonated layer were thin, it might develop local break points that keep the porosity open (Figure S7a). In addition, the mineral composition of the carbonated layer is a mixture of CaCO_3 and silicate grains, so it is possible that there are gaps along grain boundaries (Figure S7b).

Another possible explanation is related to the widely discussed inhibition of precipitation under the condition of nanoconfinement (Figure S7c,d). Precipitation may be suppressed due to the small size and curvature of the pores that increases the local surface energy.^{53,54} Alternatively, the effect may be due to the difficulty in diffusing anions through nanopores in the medium as a result of the overlap of the electrical double layer (anion exclusion), thus reducing the local saturation that drives the precipitation.⁵⁵ The pore spaces that remain unfilled could then serve as pathways for CO_2 transport if they are connected. For cementitious materials, previous studies using small-angle neutron scattering reported that the material has a pore population with ~ 5 nm diameter, in addition to the larger pore populations, and that the ~ 5 nm pores account for 1–2% of the overall porosity.^{56,57} This percentage of the small-pore population may be left unfilled during CaCO_3 precipitation.

To incorporate this nanoscale insight into the continuum model, we updated the CrunchTope software to introduce a “transport porosity”, term ϕ_t , which is the same as ϕ in eq 3 when ϕ is larger than a nonzero minimum porosity (i.e., ϕ_{\min}) but remains at ϕ_{\min} if $1 - \sum_j \phi_{mj}$ is lower than ϕ_{\min} to allow effective diffusion through the medium:

$$\phi_t = \begin{cases} 1 - \sum_j \phi_{mj}, & 1 - \sum_j \phi_{mj} > \phi_{\min} \\ \phi_{\min}, & 1 - \sum_j \phi_{mj} < \phi_{\min} \end{cases} \quad (5)$$

Because of the nonzero ϕ_{\min} , reactive fluid is still accessible by the grid cell when $1 - \sum_j \phi_{mj} > \phi_{\min}$, and thus, precipitation

reactions cannot be inhibited by lack of reactants. To avoid precipitation continuing to predict an overall mineral fraction larger than 100% of the grid volume (which is unrealistic), we introduced an inhibition of the precipitation when and only when $1 - \sum_j \phi_{mj}$ decreases to below ϕ_{\min} based on two empirical equations:

$$R' = F \times R \quad (6)$$

$$F = \begin{cases} 1, & 1 - \sum_j \phi_{mj} \geq \phi_{\min} \\ \left(\frac{1 - \sum_j \phi_{mj}}{\phi_{\min}} \right)^f, & 1 - \sum_j \phi_{mj} < \phi_{\min} \end{cases} \quad (7)$$

where F is a factor to scale down the precipitation rates to 0 when $1 - \sum_j \phi_{mj}$ approaches 0, and f is an empirical exponent (3.0 in this study).

Modeling results with the consideration of incomplete pore filling is shown in Figure 2c,d. The widening CH-depleted zone, in contrast to the base case results (Figure 2a,b), suggests that the consideration of incomplete pore filling is important for the continuous widening of the CH-depleted zone.

A minimum porosity (ϕ_{\min}) of 1.5% is used in Figure 2c,d, which was based on calibrating the new model with the experimental results using parameters specified in the **Reactive Transport Model Setup** section (see section S4 in the **Supporting Information** for more information). This porosity is comparable to the nanoporosity of the cementitious material in the small-angle neutron scattering analysis mentioned above. The minimum porosity was assumed to be constant because information about the evolution of the minimum porosity in real systems is not available.

Although the incorporation of a minimum transport porosity allows the portlandite front to continue to propagate, in agreement with the experimental data, it is not possible to reproduce the observed dissolution of the outer part of the carbonated layer (between the layer and the brine) because the brine in contact with cement is saturated with CaCO_3 (Figure S5c). The formation of the surface dissolution zone requires consideration of both nucleation of secondary CaCO_3 in brine and the enhanced CaCO_3 solubility in nanoconfinement.

Nucleation of CaCO_3 in Brine. Nucleation is the process of forming a new solid phase out of the original aqueous phase.^{58–60} It is important because nanoscale nuclei can generate a large reactive surface area,⁶¹ and the sizes of the nuclei can match that of pore throats in geomechanics, resulting in permeability reduction of the medium if the nuclei form at pore throats.⁶² Despite the importance of nucleation, it has not been fully considered in previous reactive transport models, with the exception of the work by Steefel and Van Cappellen (1990).⁵⁹ The lack of thermodynamic and kinetic parameters has certainly limited the interest in pursuing this topic in the modeling community. The common approach to nucleate new solid phases is to include a small amount of a mineral to provide sufficient surface area to start precipitation according to eq 4. This approach, however, does not always predict experimental observations well. For example, in our cement system, the brine evolved from undersaturated to oversaturated with respect to CaCO_3 during the reaction (due to CH dissolution). Even if a small amount of CaCO_3 was included in the brine domain in the initial condition to provide surface area for secondary precipitation according to eq 4, these CaCO_3

seeds would be quickly dissolved by CO₂-saturated brine before the dissolution of cement could increase the brine pH from 3 to equilibrium pH 5. Therefore, in our system, secondary CaCO₃ precipitation in brine should be initiated by nucleation.

To consider CaCO₃ nucleation in brine, the updated CrunchTope incorporates the nucleation rate equation:^{50,63–65}

$$J = J_0 \exp\left(-\frac{\Delta G^*}{kT}\right) \quad (8)$$

in which ΔG^* is expressed by

$$\Delta G^* = \frac{16\pi v^2 \alpha^3}{3k_B^2 T^2 \left[\ln\left(\frac{IAP}{K_{sp}}\right)\right]^2} \quad (9)$$

In the equations above, J_0 is a kinetic factor, ΔG^* is the nucleation energy barrier, v is the molecular volume of the nucleating phase, α is the effective interfacial energy, and k_B is the Boltzmann constant. We assume CaCO₃ nucleation takes place on an inert foreign substrate because most of the secondary CaCO₃ observed in reaction solution was on the inert Teflon liner of the reactor. Such a foreign substrate could decrease interfacial energies for nucleation (i.e., heterogeneous nucleation) relative to the case of homogeneous nucleation, in which the entire surface of the nucleus is in contact with the aqueous solution. We used v and K_{sp} for calcite (unless further modification is specified), and $\alpha = 47 \pm 1$ mJ/m² and $J_0 = 10^{-8}$ mol/m²/s, as experimentally measured from the in situ observation of CaCO₃ nucleation at nanoscale.^{65–67,77} The unit for J_0 is the moles of Ca²⁺ or CO₃^{2–} ions consumed per second from a liter of solution due to nucleation on 1 m² of a foreign substrate. A small amount of inert Teflon was added in the selected brine grids 250 μ m away from the cement domain, so that CaCO₃ could nucleate on these inert surfaces (not in other domains). To distinguish the locations where we observed the CaCO₃ in the experiment, we define the CaCO₃ in brine as CaCO_{3_in_brine} and that in cement as CaCO_{3_in_cement} in the model. At this stage, the two CaCO₃ phases are identical (in terms of molar volume, reaction formula, solubility, and molecular weight) in the database except for their names.

Figure 2e,f presents the results from a model that enabled secondary precipitation in brine via nucleation in addition to allowing effective diffusion through the carbonated layer. Although the time-resolved front depths do not differ much from those shown in Figure 2c before we incorporated the nucleation process, the mineral profile in Figure 2f clearly shows the formation of secondary CaCO₃ precipitates in brine. Due to this precipitation, the brine's CaCO₃ saturation that previously remained oversaturated (Figures S4c and S5c) drops to equilibrium (Figure S6c) with respect to both CaCO_{3_in_brine} and CaCO_{3_in_cement}. Because the CaCO_{3_in_cement} exposed to brine at the cement's surface is at equilibrium, it cannot dissolve to create a surface dissolution zone. The formation of the surface dissolution zone still requires consideration of enhanced solubility in nanopores.

Enhanced Solubility in Nanopores. The experimental observations that CaCO₃ in the cement matrix dissolves and secondary CaCO₃ precipitates in brine suggest that the CaCO₃ in the brine and that in the cement matrix have different solubilities, and this difference has to be considered in the model to reproduce the experimental observations. We hypothesized that the CaCO₃ formed in cement is more

soluble than the CaCO₃ formed in brine, such that the CaCO₃ precipitation in brine can lower the saturation with respect to CaCO₃ in cement, driving the outer front of the carbonated layer to dissolve and form a surface layer. The more soluble CaCO₃ phase in cement can be explained by (i) an altered CaCO₃ lattice size from incorporating foreign ions^{68–71} and (ii) CaCO₃ precipitation in confinement.^{53,72}

To compare the crystal lattice dimensions of CaCO₃ in cement and in brine, additional experiments were conducted for 6 and 10 days (reaction times for which we had previously observed the secondary precipitates in solution and dissolution layers on the cement surface). After the reaction, precipitates were collected from the brine and from the carbonated layer in the cement, and they were ground to powder for mineralogical analysis using XRD. The XRD results (Figure 3) show that in

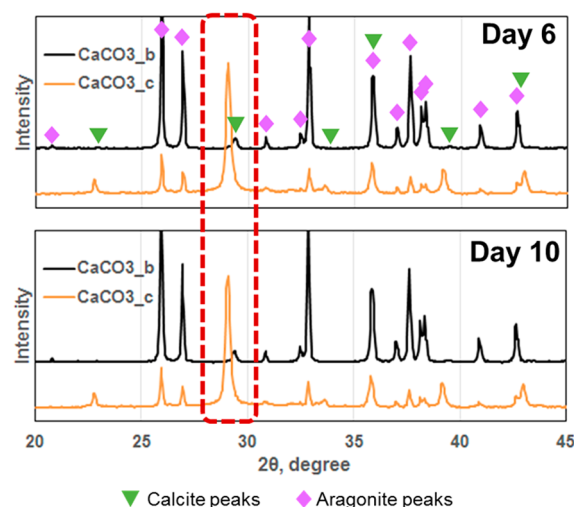


Figure 3. XRD characterization of CaCO₃ phases. In all cases, the CaCO₃ is a mixture of calcite and aragonite. All aragonite had the same lattice size, whereas the CaCO₃ in the carbonated layer in cement (or CaCO_{3_c} in legend) had larger lattices than CaCO₃ in brine (or CaCO_{3_b} in the legend). This trend is the same for the 6-day and 10-day systems. The RRUFF database was used for phase identification.

all cases, the precipitates are mixtures of aragonite and calcite. All aragonite had the same lattice dimension, whereas calcite in the cement showed peak shifts to the left of the calcite peaks for calcite in brine ($\Delta(2\theta) = 0.32^\circ$ for 6-day and 0.24° for 10-day systems), indicating that calcite in the cement has larger lattices. The larger lattices could be caused by the incorporation of foreign ions. For example, SO₄^{2–} dissolved from minor sulfate-bearing phases in cement is expected to be more concentrated in cement pore water than in brine, and it is known to increase lattice size and enhance solubility of CaCO₃ if incorporated.^{68–71}

Another potential reason for the more soluble CaCO₃ in cement is related to the crystal structure of CaCO₃ in a confined space. Precipitation in confinement requires the precipitates to be smaller and have greater surface curvature, resulting in a more-strained structure with a higher solubility compared to precipitates formed in free space.⁵³ Stephens et al. (2010) reported that in their experiment CaCO₃ precipitated in confinement was stabilized in the more-soluble form.⁷² In the cement system, CaCO_{3_in_cement} was precipitated as a dense and hard zone, suggesting that CaCO₃ was precipitated in

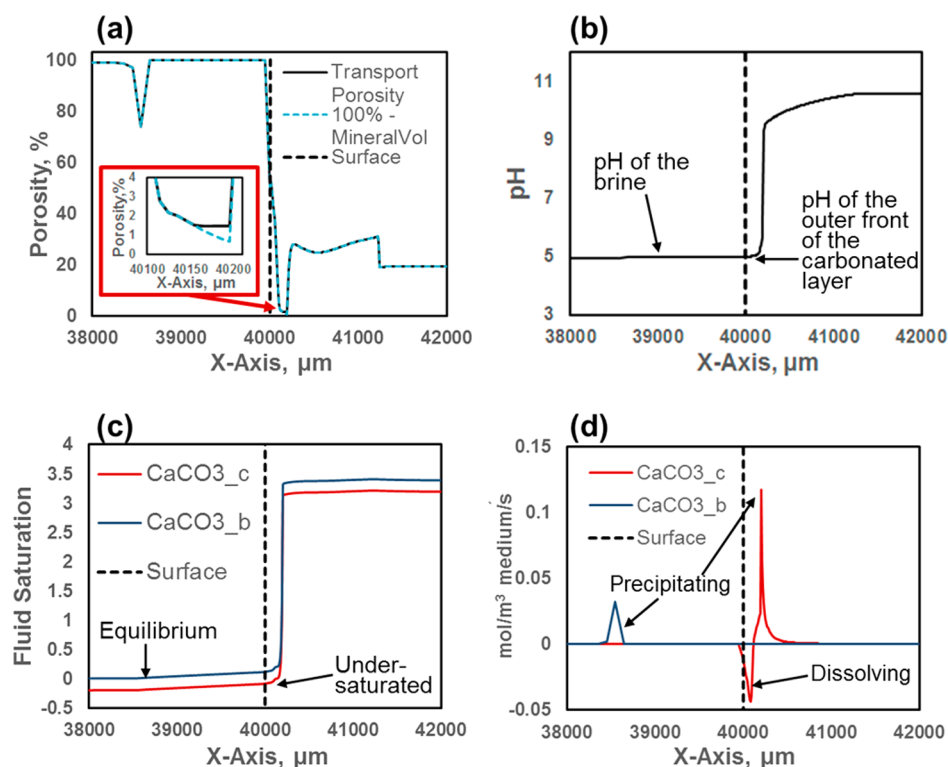


Figure 4. Plots of modeling results for day-10. (a) Porosity profiles that compares the porosity for transport (ϕ_t in eq 5) and the value of $1 - \sum_j \phi_{mj}$. The nonzero ϕ_t allows effective diffusion through the carbonated layer. (b) pH profile. The pH is equilibrated at 5 outside of the carbonated layer and is above 9 inside of the carbonated layer. (c) Saturation profiles for CaCO_3 in brine and CaCO_3 in cement. Precipitation of CaCO_3 in brine decreases brine saturation to the point of being undersaturated with CaCO_3 in cement. (d) Reaction rates for CaCO_3 in brine and CaCO_3 in cement. Positive values indicate precipitation and negative values indicate dissolution.

confined spaces, potentially creating a more-soluble form than CaCO_3 in brine.

To avoid complications by introducing distinct CaCO_3 polymorphs, we treated the calcite–aragonite mixture as a single CaCO_3 phase and used two different calcite K_{sp} values for CaCO_3 in brine ($K_{sp} = 10^{-9.23}$ at 95 °C) and CaCO_3 in cement ($K_{sp} = 10^{-9.03}$ at 95 °C), with the $\log_{10} K_{sp}$ of CaCO_3 in cement assumed to be 0.2 higher. This $\log_{10} K_{sp}$ difference is similar to that between calcite and aragonite, large enough to distinguish two phases and small enough to allow coexistence in one system. The inclusion of two CaCO_3 solubilities in our model allows the dissolution of the cement surface layer to be predicted (Figure 2g,h) because the precipitation of CaCO_3 in brine can drive the brine to be undersaturated with respect to the more-soluble CaCO_3 in cement.

Summary of Improved Simulation with Nanoscale Mechanisms. After all of the nanoscale mechanisms discussed above were incorporated, the modeling results successfully captured the evolution of the CH-depleted zone and the surface dissolution zone, as shown in Figure 2g. The mineral profile in Figure 2h shows that the secondary CaCO_3 phase in brine is captured and that minor secondary C–S–H phases are formed in the CH-depleted zone. The surface dissolution zone is attributed to the dissolution of CaCO_3 , not silica.

The newly incorporated nanoscale mechanisms are reflected in the detailed modeling results for day-10 as an example reaction time, shown in Figure 4 (corresponding results for cases without sufficient consideration of nanoscale mechanisms are shown in Figures S4–6). Figure 4a indicates that the porosity in the CH-depleted zone increases despite the

secondary C–S–H formation and that diffusion through the carbonate layer was still effective via the “transport porosity” that represents the pore space unable to be filled by precipitates. Detailed discussion on parameters in the model can be found in section S4 of the Supporting Information. Figure 4b shows that the pH is equilibrated at 5 outside of the carbonated layer and is above 9 inside of the carbonated layer. This means that the CaCO_3 in brine and the CaCO_3 in cement on the outer surface of the carbonated layer experiences the same pH environment. Figure 4c,d shows that precipitation of CaCO_3 in brine decreases brine saturation for CaCO_3 in cement and allows it to dissolve at the outer front of the carbonated layer, while the inner front of the carbonated layer experiences rapid CaCO_3 precipitation.

ENVIRONMENTAL IMPLICATIONS

This work provides insights into the effects of nanoscale mechanisms during deterioration of wellbore cement, which is of importance for safer and more-efficient CO_2 storage and other energy-related subsurface operations. It can serve as an example case that proves the importance of nanoscale mechanisms in affecting macroscale phenomena. Furthermore, the new features in the current version of CrunchTope enable it to better describe systems in experiments and real-world applications.

This study also suggests potential engineering strategies to mitigate cement deterioration. We showed that porosity in the carbonated layer can have a significant impact on widening of the weak CH-depleted zone. The protective efficiency of the carbonated layer can be improved (and, thus, widening of the

CH-depleted zone can be prevented) by promoting less-defective grain boundaries, by forming a thicker carbonated layer, and by diminishing the pore-size dependency of CaCO_3 precipitation. We also showed that the outer front of the carbonated layer can dissolve if its solubility is higher than the secondary CaCO_3 in brine. One potential strategy to avoid excessive cement deterioration is to intentionally adjust the fluid chemistry with certain reactive ions, such as SO_4^{2-} and Mg^{2+} , to increase solubility of the CaCO_3 phase in the brine and, thus, decrease solubility difference between CaCO_3 in cement and in brine.^{68–71}

Further, the roles of nanoscale mechanisms revealed in this study help us understand subsurface reactive systems better. For example, our previous study on cement deterioration introduced 50 mM of sulfate ions in the reaction brine and found that the CO_2 attack on cement was mitigated significantly.²⁶ That study experimentally verified that this mitigation was due to less cement surface dissolution as a result of sulfate mineral precipitation or ion adsorption on CaCO_3 grains. Utilizing the findings of the current study, we can offer two additional possible explanations: First, sulfate ions can decrease the CaCO_3 precipitation rate in cement, allowing more time for ions to diffuse into pores and arrange more-crystalline structures. Second, when the sulfate ion concentration is comparatively high in the brine (although still undersaturated with respect to CaSO_4), CaCO_3 in brine can incorporate sulfate ions, making the resulting CaCO_3 more soluble. Then the difference between the solubility of CaCO_3 in brine and the CaCO_3 in cement became smaller, and the dissolution of the CaCO_3 in cement is slowed down.

■ ASSOCIATED CONTENT

■ Supporting Information

The Supporting Information is available free of charge on the ACS Publications website at DOI: 10.1021/acs.est.7b00594.

Additional details, tables, and figures showing an estimation of description of the CaCO_3 phase-comparison experiments, initial conditions for the cement domain, additional results, and discussion on modeling parameters. (PDF)

■ AUTHOR INFORMATION

Corresponding Author

*Phone: (314) 935-4539. Fax: (314) 935-7211. E-mail: ysjun@seas.wustl.edu.

ORCID

Young-Shin Jun: 0000-0003-4648-2984

Notes

The authors declare no competing financial interest.

■ ACKNOWLEDGMENTS

This work was supported by the Center for Nanoscale Control of Geologic CO_2 , an Energy Frontier Research Center funded by the U.S. Department of Energy, Office of Science, Office of Basic Energy Sciences, under award no. DE-AC02-05CH11231.

■ REFERENCES

(1) Gasda, S. E.; Bachu, S.; Celia, M. A. Spatial Characterization of the Location of Potentially Leaky Wells Penetrating a Deep Saline Aquifer in a Mature Sedimentary Basin. *Environ. Geol.* **2004**, *46* (6–7), 707–720.

(2) Nordbotten, J. M.; Celia, M. A.; Bachu, S.; Dahle, H. K. Semianalytical Solution for CO_2 Leakage through an Abandoned Well. *Environ. Sci. Technol.* **2005**, *39* (2), 602–611.

(3) Carey, J. W. Geochemistry of Wellbore Integrity in CO_2 Sequestration: Portland Cement-steel-brine- CO_2 Interactions. *Rev. Mineral. Geochem.* **2013**, *77* (1), 505–539.

(4) Abdoulghafour, H.; Gouze, P.; Luquot, L.; Leprovost, R. Characterization and Modeling of the Alteration of Fractured Class-G Portland Cement During Flow of CO_2 -Rich Brine. *Int. J. Greenhouse Gas Control* **2016**, *48*, 155–170.

(5) Brunet, J.-P. L.; Li, L.; Karpyn, Z. T.; Kutchko, B. G.; Strazisar, B.; Bromhal, G. Dynamic Evolution of Cement Composition and Transport Properties under Conditions Relevant to Geological Carbon Sequestration. *Energy Fuels* **2013**, *27* (8), 4208–4220.

(6) Fabbri, A.; Corvisier, J.; Schubnel, A.; Brunet, F.; Goffé, B.; Rimmele, G.; Barlet-Gouédard, V. Effect of Carbonation on the Hydro-Mechanical Properties of Portland Cements. *Cem. Concr. Res.* **2009**, *39* (12), 1156–1163.

(7) Gherardi, F.; Audigane, P.; Gaucher, E. C. Predicting Long-term Geochemical Alteration of Wellbore Cement in a Generic Geological CO_2 Confinement Site: Tackling a Difficult Reactive Transport Modeling Challenge. *J. Hydrol.* **2012**, *420*, 340–359.

(8) Huet, B. M.; Prevost, J. H.; Scherer, G. W. Quantitative Reactive Transport Modeling of Portland Cement in CO_2 -saturated Water. *Int. J. Greenhouse Gas Control* **2010**, *4* (3), 561–574.

(9) Kutchko, B. G.; Strazisar, B. R.; Dzombak, D. A.; Lowry, G. V.; Thaulow, N. Degradation of Well Cement by CO_2 under Geologic Sequestration Conditions. *Environ. Sci. Technol.* **2007**, *41* (13), 4787–4792.

(10) Kutchko, B. G.; Strazisar, B. R.; Lowry, G. V.; Dzombak, D. A.; Thaulow, N. Rate of CO_2 Attack on Hydrated Class H Well Cement under Geologic Sequestration Conditions. *Environ. Sci. Technol.* **2008**, *42* (16), 6237–6242.

(11) Li, Q.; Lim, Y. M.; Flores, K. M.; Kranjc, K.; Jun, Y.-S. Chemical Reactions of Portland Cement with Aqueous CO_2 and Their Impacts on Cement's Mechanical Properties under CO_2 Sequestration Conditions. *Environ. Sci. Technol.* **2015**, *49* (10), 6335–6343.

(12) Zhang, L.; Dzombak, D. A.; Nakles, D. V.; Hawthorne, S. B.; Miller, D. J.; Kutchko, B. G.; Lopano, C. L.; Strazisar, B. R. Rate of H_2S and CO_2 Attack on Pozzolan-Amended Class H Well Cement under Geologic Sequestration Conditions. *Int. J. Greenhouse Gas Control* **2014**, *27*, 299–308.

(13) Duguid, A.; Radonjic, M.; Scherer, G. W. Degradation of Cement at the Reservoir/Cement Interface from Exposure to Carbonated Brine. *Int. J. Greenhouse Gas Control* **2011**, *5* (6), 1413–1428.

(14) Kutchko, B. G.; Strazisar, B. R.; Huerta, N.; Lowry, G. V.; Dzombak, D. A.; Thaulow, N. CO_2 Reaction with Hydrated Class H Well Cement under Geologic Sequestration Conditions: Effects of Flyash Admixtures. *Environ. Sci. Technol.* **2009**, *43* (10), 3947–3952.

(15) Jung, H. B.; Um, W. Experimental Study of Potential Wellbore Cement Carbonation by Various Phases of Carbon Dioxide during Geologic Carbon Sequestration. *Appl. Geochem.* **2013**, *35*, 161–172.

(16) Huerta, N. J.; Hesse, M. A.; Bryant, S. L.; Strazisar, B. R.; Lopano, C. L. Experimental Evidence for Self-limiting Reactive Flow Through a Fractured Cement Core: Implications for Time-dependent Wellbore Leakage. *Environ. Sci. Technol.* **2013**, *47* (1), 269–275.

(17) Newell, D. L.; Carey, J. W. Experimental Evaluation of Wellbore Integrity Along the Cement-Rock Boundary. *Environ. Sci. Technol.* **2013**, *47* (1), 276–282.

(18) Walsh, S. D.; Du Frane, W. L.; Mason, H. E.; Carroll, S. A. Permeability of Wellbore-Cement Fractures Following Degradation by Carbonated Brine. *Rock Mech Rock Eng.* **2013**, *46* (3), 455–464.

(19) Abdoulghafour, H.; Luquot, L.; Gouze, P. Characterization of the Mechanisms Controlling the Permeability Changes of Fractured Cements Flowed through by CO_2 -rich Brine. *Environ. Sci. Technol.* **2013**, *47* (18), 10332–10338.

- (20) Matteo, E. N.; Scherer, G. W. Experimental Study of the Diffusion-Controlled Acid Degradation of Class H Portland Cement. *Int. J. Greenhouse Gas Control* **2012**, *7*, 181–191.
- (21) Wigand, M.; Kaszuba, J. P.; Carey, J. W.; Hollis, W. K. Geochemical Effects of CO₂ Sequestration on Fractured Wellbore Cement at the Cement/Caprock Interface. *Chem. Geol.* **2009**, *265* (1), 122–133.
- (22) Mason, H. E.; Du Frane, W. L.; Walsh, S. D.; Dai, Z.; Charnvanichborikarn, S.; Carroll, S. A. Chemical and Mechanical Properties of Wellbore Cement Altered by CO₂-rich Brine using a Multianalytical Approach. *Environ. Sci. Technol.* **2013**, *47* (3), 1745–1752.
- (23) Zhang, L.; Dzombak, D. A.; Nakles, D. V.; Hawthorne, S. B.; Miller, D. J.; Kutcho, B. G.; Lopano, C. L.; Strazisar, B. R. Characterization of Pozzolan-Amended Wellbore Cement Exposed to CO₂ and H₂S Gas Mixtures under Geologic Carbon Storage Conditions. *Int. J. Greenhouse Gas Control* **2013**, *19*, 358–368.
- (24) Walsh, S. D.; Mason, H. E.; Du Frane, W. L.; Carroll, S. A. Mechanical and Hydraulic Coupling in Cement–Caprock Interfaces Exposed to Carbonated Brine. *Int. J. Greenhouse Gas Control* **2014**, *25*, 109–120.
- (25) Hangx, S. J.; Linden, A. v. d.; Marcelis, F.; Liteanu, E. Defining the Brittle Failure Envelopes of Individual Reaction Zones Observed in CO₂-Exposed Wellbore Cement. *Environ. Sci. Technol.* **2016**, *50* (2), 1031–1038.
- (26) Li, Q.; Lim, Y. M.; Jun, Y.-S. Effects of Sulfate during CO₂ Attack on Portland Cement and Their Impacts on Mechanical Properties under Geologic CO₂ Sequestration Conditions. *Environ. Sci. Technol.* **2015**, *49* (11), 7032–7041.
- (27) Walsh, S. D.; Mason, H. E.; Du Frane, W. L.; Carroll, S. A. Experimental Calibration of a Numerical Model Describing the Alteration of Cement/Caprock Interfaces by Carbonated Brine. *Int. J. Greenhouse Gas Control* **2014**, *22*, 176–188.
- (28) Cao, P.; Karpyn, Z.; Li, L. Dynamic Changes in Wellbore Cement Integrity Due to Geochemical Reactions in CO₂-rich Environments. *Water Resour. Res.* **2013**, *49*, 4465–4475.
- (29) Carey, J. W.; Svec, R.; Grigg, R.; Zhang, J.; Crow, W. Experimental Investigation of Wellbore Integrity and CO₂–Brine Flow Along the Casing–Cement Microannulus. *Int. J. Greenhouse Gas Control* **2010**, *4* (2), 272–282.
- (30) Duguid, A.; Scherer, G. W. Degradation of Oilwell Cement due to Exposure to Carbonated Brine. *Int. J. Greenhouse Gas Control* **2010**, *4* (3), 546–560.
- (31) Wilkins, S. J.; Compton, R. G.; Taylor, M. A.; Viles, H. A. Channel Flow Cell Studies of the Inhibiting Action of Gypsum on the Dissolution Kinetics of Calcite: A Laboratory Approach With Implications for Field Monitoring. *J. Colloid Interface Sci.* **2001**, *236* (2), 354–361.
- (32) Wolterbeek, T. K.; Peach, C. J.; Spiers, C. J. Reaction and Transport in Wellbore Interfaces under CO₂ Storage Conditions: Experiments Simulating Debonded Cement–Casing Interfaces. *Int. J. Greenhouse Gas Control* **2013**, *19*, 519–529.
- (33) Barlet-Gouédard, V.; Rimmelé, G.; Porcherie, O.; Quisel, N.; Desroches, J. A Solution Against Well Cement Degradation under CO₂ Geological Storage Environment. *Int. J. Greenhouse Gas Control* **2009**, *3* (2), 206–216.
- (34) Jacquemet, N.; Pironon, J.; Saint-Marc, J. Mineralogical Changes of a Well Cement in Various H₂S–CO₂ (–brine) Fluids at High Pressure and Temperature. *Environ. Sci. Technol.* **2008**, *42* (1), 282–288.
- (35) Jung, H. B.; Jansik, D.; Um, W. Imaging Wellbore Cement Degradation by Carbon Dioxide under Geologic Sequestration Conditions using X-Ray Computed Microtomography. *Environ. Sci. Technol.* **2013**, *47* (1), 283–289.
- (36) Kutcho, B. G.; Strazisar, B. R.; Hawthorne, S. B.; Lopano, C. L.; Miller, D. J.; Hakala, J. A.; Guthrie, G. D. H₂S–CO₂ Reaction with Hydrated Class H Well Cement: Acid-gas Injection and CO₂ Co-Sequestration. *Int. J. Greenhouse Gas Control* **2011**, *5* (4), 880–888.
- (37) Fabbri, A.; Jacquemet, N.; Seyedi, D. A Chemo-Poromechanical Model of Oilwell Cement Carbonation under CO₂ Geological Storage Conditions. *Cem. Concr. Res.* **2012**, *42* (1), 8–19.
- (38) Gherardi, F.; Audigane, P. Modeling Geochemical Reactions in Wellbore Cement: Assessing Pre-injection Integrity in a Site for CO₂ Geological Storage. *Greenhouse Gases: Sci. Technol.* **2013**, *3* (6), 447–474.
- (39) Zhang, L.; Dzombak, D. A.; Nakles, D. V.; Brunet, J.-P. L.; Li, L. Reactive Transport Modeling of Interactions between Acid Gas (CO₂ + H₂S) and Pozzolan-Amended Wellbore Cement under Geologic Carbon Sequestration Conditions. *Energy Fuels* **2013**, *27* (11), 6921–6937.
- (40) Brunet, J.-P. L.; Li, L.; Karpyn, Z. T.; Huerta, N. J. Fracture Opening or Self-Sealing: Critical Residence Time as a Unifying Parameter for Cement–CO₂–Brine Interactions. *Int. J. Greenhouse Gas Control* **2016**, *47*, 25–37.
- (41) Marty, N. C.; Tournassat, C.; Burnol, A.; Giffaut, E.; Gaucher, E. C. Influence of Reaction Kinetics and Mesh Refinement on the Numerical Modelling of Concrete/Clay Interactions. *J. Hydrol.* **2009**, *364* (1), 58–72.
- (42) Raoof, A.; Nick, H.; Wolterbeek, T.; Spiers, C. Pore-Scale Modeling of Reactive Transport in Wellbore Cement under CO₂ Storage Conditions. *Int. J. Greenhouse Gas Control* **2012**, *11*, S67–S77.
- (43) Mahmoudzadeh, B.; Liu, L.; Moreno, L.; Neretnieks, I. Solute Transport in Fractured Rocks with Stagnant Water Zone and Rock Matrix Composed of Different Geological Layers—Model Development and Simulations. *Water Resour. Res.* **2013**, *49* (3), 1709–1727.
- (44) Steefel, C. I. *Crunchflow Software for Modeling Multicomponent Reactive Flow and Transport. User's Manual*; Lawrence Berkeley National Laboratory: Berkeley, CA, 2015.
- (45) Taylor, H. F. *Cement Chemistry*; Thomas Telford: London, U.K., 1997.
- (46) Duan, Z.; Sun, R. An Improved Model Calculating CO₂ Solubility in Pure Water and Aqueous NaCl Solutions from 273 to 533 K and from 0 to 2000 bar. *Chem. Geol.* **2003**, *193* (3), 257–271.
- (47) Holzbecher, E. *Environmental Modeling: using MATLAB*; Springer Science & Business Media: Berlin, Germany, 2012.
- (48) Wolery, T. J. *EQ3/6: A Software Package for Geochemical Modeling of Aqueous Systems: Package Overview and Installation Guide*, version 7.0; Lawrence Livermore National Laboratory: Livermore, CA, 1992.
- (49) BRGM. Thermodem: Thermochemical and Mineralogical Tables for Geochemical Modeling. <http://thermodem.brgm.fr/> (accessed July 25, 2012).
- (50) Lasaga, A. C. *Kinetic Theory in the Earth Sciences*; Princeton University Press: Princeton, NJ, 1998.
- (51) Steefel, C. I.; DePaolo, D. J.; Lichtner, P. C. Reactive Transport Modeling: An Essential Tool and a New Research Approach for the Earth sciences. *Earth Planet. Sci. Lett.* **2005**, *240* (3), 539–558.
- (52) Neuville, N.; Lécuyer, E.; Aouad, G.; Rivereau, A.; Damidot, D. Effect of Curing Conditions on Oilwell Cement Paste Behaviour during Leaching: Experimental and Modelling Approaches. *C. R. Chim.* **2009**, *12* (3), 511–520.
- (53) Stack, A. G. Precipitation in Pores: A Geochemical Frontier. *Rev. Mineral. Geochem.* **2015**, *80*, 165–190.
- (54) Emmanuel, S.; Ague, J. J.; Walderhaug, O. Interfacial Energy Effects and the Evolution of Pore Size Distributions during Quartz Precipitation in Sandstone. *Geochim. Cosmochim. Acta* **2010**, *74* (12), 3539–3552.
- (55) Chagneau, A. I.; Tournassat, C.; Steefel, C. I.; Bourg, I. C.; Gaboreau, S. p.; Esteve, I. n.; Kupcik, T.; Claret, F.; Schäfer, T. Complete Restriction of ³⁶Cl–Diffusion by Celestite Precipitation in Densely Compacted Illite. *Environ. Sci. Technol. Lett.* **2015**, *2* (5), 139–143.
- (56) Pearson, D.; Allen, A.; Windsor, C.; Alford, M. N.; Double, D. An Investigation on the Nature of Porosity in Hardened Cement Pastes using Small Angle Neutron Scattering. *J. Mater. Sci.* **1983**, *18* (2), 430–438.

- (57) Allen, A.; Windsor, C.; Rainey, V.; Pearson, D.; Double, D.; Alford, N. M. A Small-Angle Neutron Scattering Study of Cement Porosities. *J. Phys. D: Appl. Phys.* **1982**, *15* (9), 1817.
- (58) Thomas, J. J. A New Approach to Modeling the Nucleation and Growth Kinetics of Tricalcium Silicate Hydration. *J. Am. Ceram. Soc.* **2007**, *90* (10), 3282–3288.
- (59) Steefel, C. I.; Van Cappellen, P. A New Kinetic Approach to Modeling Water-rock Interaction: The Role of Nucleation, Precursors, and Ostwald Ripening. *Geochim. Cosmochim. Acta* **1990**, *54* (10), 2657–2677.
- (60) Thomas, J. J.; Jennings, H. M.; Chen, J. J. Influence of Nucleation Seeding on the Hydration Mechanisms of Tricalcium Silicate and Cement. *J. Phys. Chem. C* **2009**, *113* (11), 4327–4334.
- (61) Noiriél, C.; Steefel, C. I.; Yang, L.; Ajo-Franklin, J. Upscaling Calcium Carbonate Precipitation Rates from Pore to Continuum Scale. *Chem. Geol.* **2012**, *318*, 60–74.
- (62) Shao, C.; Yang, Z.; Zhou, G.; Lu, G. Pore Network Modeling of Water Block in Low Permeability Reservoirs. *Pet. Sci.* **2010**, *7* (3), 362–366.
- (63) De Yoreo, J. J.; Vekilov, P. G. Principles of Crystal Nucleation and Growth. *Rev. Mineral. Geochem.* **2003**, *54* (1), 57–93.
- (64) De Yoreo, J. J.; Waychunas, G. A.; Jun, Y.-S.; Fernandez-Martinez, A. *In Situ* Investigations of Carbonate Nucleation on Mineral and Organic Surfaces. *Rev. Mineral. Geochem.* **2013**, *77* (1), 229–257.
- (65) Li, Q.; Jun, Y.-S. Heterogeneous Calcium Carbonate Nucleation in Saline Solution: Thermodynamic and Kinetic Contributions. In Proceedings of 251st ACS National Meeting, San Diego, CA, March 13–17, 2016.
- (66) Li, Q.; Fernandez-Martinez, A.; Lee, B.; Waychunas, G. A.; Jun, Y.-S. Interfacial Energies for Heterogeneous Nucleation of Calcium Carbonate on Mica and Quartz. *Environ. Sci. Technol.* **2014**, *48* (10), 5745–5753.
- (67) Li, Q. *Calcium Carbonate Formation in Energy-Related Subsurface Environments and Engineered Systems*; Washington University in St. Louis: St. Louis, MO, 2016.
- (68) He, S.; Morse, J. W. The Carbonic Acid System and Calcite Solubility in Aqueous Na-K-Ca-Mg-Cl-SO₄ Solutions From 0 to 90 °C. *Geochim. Cosmochim. Acta* **1993**, *57* (15), 3533–3554.
- (69) Gledhill, D. K.; Morse, J. W. Calcite Solubility in Na–Ca–Mg–Cl Brines. *Chem. Geol.* **2006**, *233* (3), 249–256.
- (70) Akin, G.; Lagerwerff, J. Calcium Carbonate Equilibria in Solutions Open to the Air. II. Enhanced Solubility of CaCO₃ in the Presence of Mg²⁺ and SO₄²⁻. *Geochim. Cosmochim. Acta* **1965**, *29* (4), 353–360.
- (71) Chong, T.; Sheikholeslami, R. Thermodynamics and Kinetics for Mixed Calcium Carbonate and Calcium Sulfate Precipitation. *Chem. Eng. Sci.* **2001**, *56* (18), 5391–5400.
- (72) Stephens, C. J.; Ladden, S. F.; Meldrum, F. C.; Christenson, H. K. Amorphous Calcium Carbonate is Stabilized in Confinement. *Adv. Funct. Mater.* **2010**, *20* (13), 2108–2115.
- (73) De Windt, L.; Marsal, F.; Tinseau, E.; Pellegrini, D. Reactive Transport Modeling of Geochemical Interactions at a Concrete/Argillite Interface, Tournemire Site (France). *Phys. Chem. Earth* **2008**, *33*, S295–S305.
- (74) Palandri, J. L.; Kharaka, Y. K. *A Compilation of Rate Parameters of Water-Mineral Interaction Kinetics for Application to Geochemical Modeling*; DTIC: Fort Belvoir, VA, 2004.
- (75) Wertz, F.; Gherardi, F.; Blanc, P.; Bader, A.; Fabbri, A. In *Modeling CO₂-Driven Cement Alteration at Well-Caprock Interface*, Proceedings of TOUGH Symposium, Sept 17–19, 2012.
- (76) Jun, Y.-S.; Zhang, L.; Min, Y.; Li, Q. Nanoscale Chemical Processes Affecting Storage Capacities and Seals during Geologic CO₂ Sequestration. *Acc. Chem. Res.* **2017**, *50* (7), 1521–1529.
- (77) Li, Q.; Jun, Y.-S. In *Experimental Quantification of the Kinetic Factor in the Nucleation Rate Equation*, 253rd ACS National Meeting, San Francisco, USA, 2017.